Ecological Indicators 150 (2023) 110190

Contents lists available at ScienceDirect

Ecological Indicators

journal homepage: www.elsevier.com/locate/ecolind

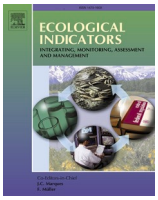

Drone lidar-derived surface complexity metrics as indicators of intertidal oyster reef condition

Michael C. Espriella [a,*], Vincent Lecours [a,b], Edward V. Camp [a], H. Andrew Lassiter [a], Benjamin Wilkinson [a], Peter C. Frederick [c], Simon J. Pittman [d]

[a] School of Forest, Fisheries, and Geomatics Sciences, University of Florida, Gainesville, FL, USA
[b] Université du Québec à Chicoutimi, Saguenay, QC, Canada
[c] Department of Wildlife Ecology and Conservation, University of Florida, Gainesville, FL, USA
[d] Oxford Seascape Ecology Lab, School of Geography and the Environment, University of Oxford, OX1 3QY, United Kingdom

ARTICLE INFO

Keywords:
UAV
UAS
Rugosity
Geomorphometry
Coastal habitat
Remote sensing

ABSTRACT

Eastern oysters (*Crassostrea virginica*) generate structurally complex reef systems that offer diverse ecosystem services. However, there is limited understanding of how reef structure translates into reef condition. This knowledge gap might be better addressed if oyster reef structure could be more rapidly assessed. Conventional *in situ* monitoring techniques are often time-intensive, invasive, and do not provide spatially continuous information on the reef structure. Unoccupied Aircraft Systems (UAS), commonly referred to as drones, equipped with optical sensors can rapidly and non-invasively map intertidal oyster reef surfaces. We demonstrate how a digital surface model from UAS-based light detection and ranging (lidar) can enable very high-resolution characterization and monitoring of intertidal oyster reef surface morphology. Generalized linear models (GLMs) identified relationships between *in situ* live oyster counts and surface complexity metrics derived from digital surface models produced from lidar point clouds. Statistically significant relationships between surface complexity metrics (e.g., gray level co-occurrence features, volume to area ratio, skewness of elevation) and live oyster counts suggest that surface complexity provides useful proxies for reef condition. Advancing the application of remote sensing to intertidal oyster reefs can help identify reefs that are prone to degradation and inform conservation and restoration strategies.

1. Introduction

Eastern oysters (*Crassostrea virginica*) and the reef structures they form provide valuable ecosystem services such as water filtration and shoreline erosion control (Coen et al., 2007; Grabowski & Peterson, 2007). However, stressors such as overharvest, disease, and an increasing frequency of drought conditions have resulted in declining oyster populations and reef coverage both globally (Grabowski & Peterson, 2007; Beck et al., 2011) and locally in places like Florida, USA (Seavey et al. 2011; Frederick et al., 2016). Despite the decline in oyster reefs, and the consequences to coastal communities and estuarine ecosystems alike, there is still limited understanding of how to monitor these habitats consistently and effectively (Baggett et al. 2015; NAS 2017; La Peyre et al. 2022). Conventional field methods for monitoring intertidal oyster reefs that require researchers to access reefs directly are time-intensive, constrained by access at low tide, and are often invasive. In addition, *in situ* sampling using transects or quadrats is typically too fine-scale relative to the spatial extent of oyster reefs. Furthering our understanding of these systems by developing novel and rapid monitoring methods that acquire spatially continuous data at operationally relevant scales for decision-making will support conservation and restoration efforts.

Unoccupied Aircraft Systems (UAS), commonly known as drones, provide an alternative to conventional sampling methods, allowing for rapid data collection over multiple intertidal reefs in one survey. Using UAS to study intertidal oyster reefs also minimizes impact on the reefs by reducing the need for *in situ* field sampling. Additionally, sensors mounted on UAS enable continuous characterization of the reef surface, rather than the limited sample areas typical of field monitoring methods. There are now a multitude of optical sensor payloads such as lidar, multispectral cameras, and hyperspectral cameras that can be utilized depending upon the objective and budget of the monitoring program or

* Corresponding author at: 406 Reed Lab, PO Box 110565, Gainesville, FL 32611-0565, USA.
E-mail address: michaelespriella@ufl.edu (M.C. Espriella).

https://doi.org/10.1016/j.ecolind.2023.110190
Received 16 December 2022; Received in revised form 22 March 2023; Accepted 24 March 2023
Available online 10 April 2023

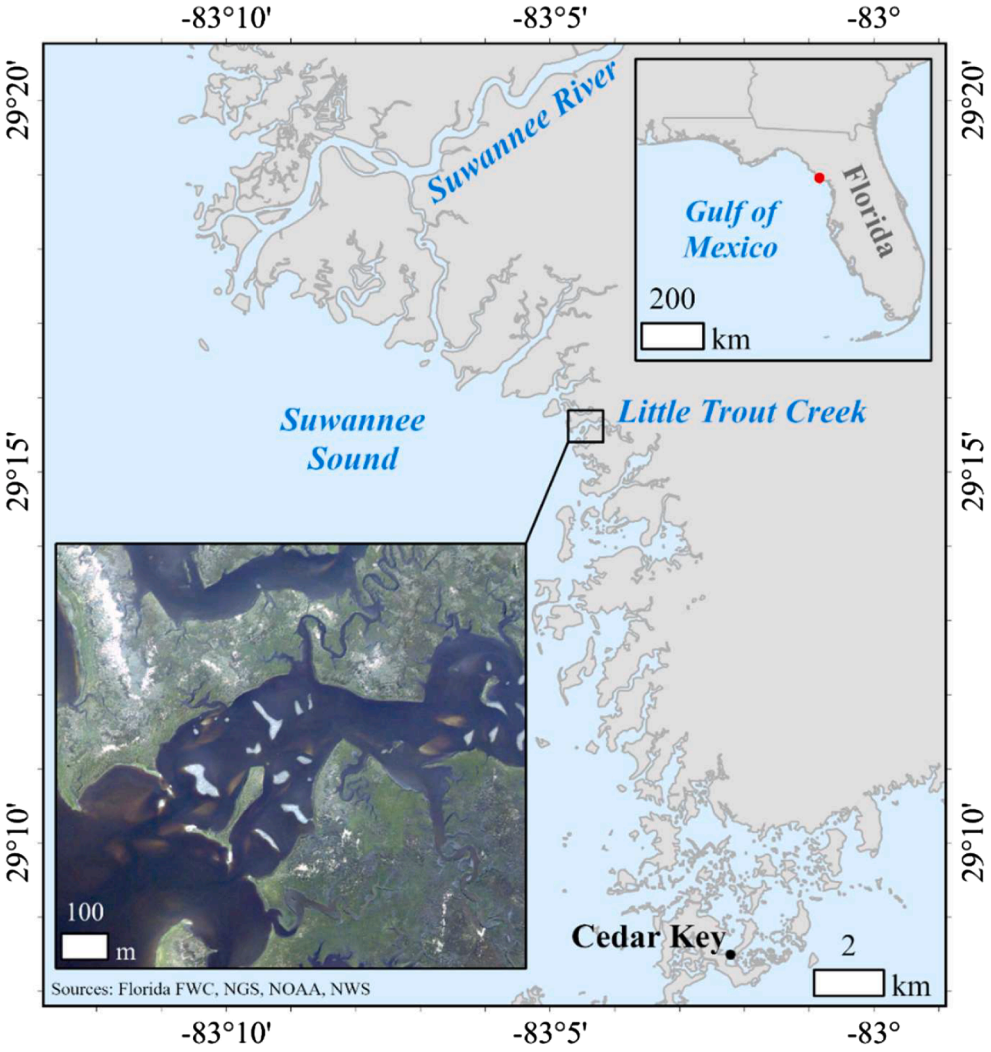

Fig. 1. Location of the study site and aerial photo showing the Little Trout Creek tidal system in October 2018.

research project (Baxter & Hamilton, 2018; Collin et al., 2018; Johnston, 2019; Brunier et al., 2022). Researchers have used UAS to study intertidal reefs in a variety of contexts, including reef morphology (Windle et al., 2019), reef detection (Ridge et al., 2020), and estuarine habitat classification (Espriella et al., 2020; Chand & Bollard, 2021; Espriella & Lecours, 2022). Despite these advances, significant challenges remain regarding what information derived from UAS data products best characterizes intertidal oyster reefs, as well as what metrics provide an ecologically meaningful linkage between intertidal oyster reef condition and biophysical reef structure. There is no standardized metric or method to measure reef condition (Baggett et al. 2015; NAS 2017), and as autogenic ecosystem engineers, oyster reef structure is inherently connected to condition given the structure is living and serves as substrate for settlement (Wilberg et al., 2013; Johnson et al., 2022).

One product that can be derived from UAS surveys and is often underutilized in monitoring contexts is a digital surface model (DSM), which provides detailed elevation data from which terrain characteristics that quantify surface morphology can be derived. DSMs can be generated using lidar point clouds or by applying Structure from Motion (SfM) photogrammetry techniques to spectral imagery (Carrivick & Smith, 2019). SfM is a procedure in which overlapping images are used to reconstruct the 3-D structure of a surveyed scene (Iglhaut et al., 2019). DSMs can provide information characterizing structural traits of oyster reefs which can influence the surrounding physical environment (Chowdhury et al., 2019). DSMs also allow analysis of oyster reefs from a geomorphometric (i.e., the quantitative analysis of land surfaces) perspective by generating terrain attributes such as rugosity and curvature (Hengl & Reuter, 2008; Lecours et al., 2016; Florinsky, 2017).

Habitat complexity metrics such as rugosity have often been associated with higher levels of biodiversity in the marine environment (Pittman et al. 2007; Dunn & Halpin, 2009; Harborne et al., 2012; Dustan et al., 2013; Nugraha et al., 2020). However, the studies that establish these relationships are largely conducted on coral reefs and are typically interested in explaining fish distributions rather than the condition of the biogenic structure itself (Burns et al., 2015). Furthermore, when oyster reef rugosity is considered, it is often calculated using a conventional method such as the chain method (i.e., conforming a chain to the structure and dividing the conformed length by the linear length on a given transect), which does not provide a continuous depiction of complexity, as is available with DSMs (Margiotta et al., 2016; Colden et al., 2017).

Reef structure and complexity carries relationships with the condition of the reef as live oysters are typically vertically oriented and structural complexity can increase oyster survivorship (Sonnier, 2006; Hanke et al., 2017; Windle et al., 2022). Oyster reef vertical complexity is a potential ecological indicator for oyster reef condition and is also relevant to organisms that inhabit reefs (Howie & Bishop, 2021). For those that inhabit oyster reefs, vertical complexity can offer refuge from predation (Margiotta et al., 2016). For oysters themselves, vertical complexity can enhance recruitment (Soniat et al., 2004; Nestlerode

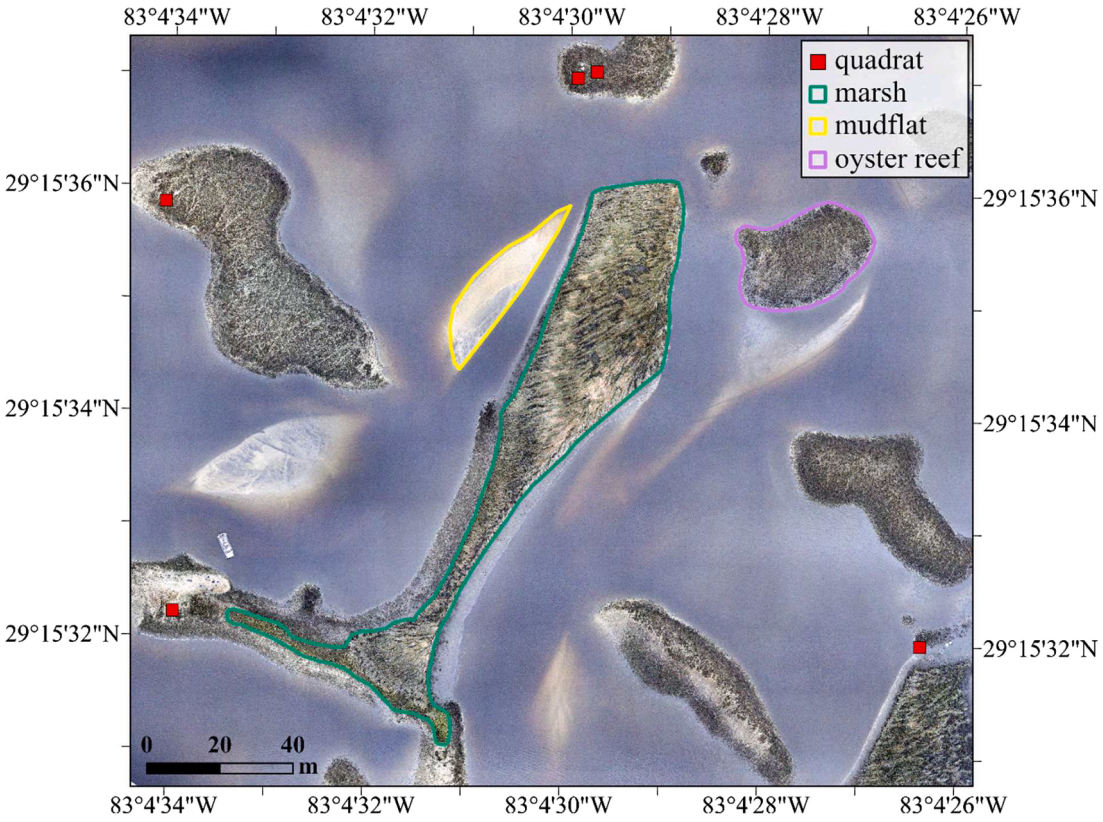

Fig. 2. Placement of the quadrats overlaid on 2 cm resolution UAS imagery collected simultaneously with the lidar data. An example for each habitat cover is also delineated.

et al., 2007; Margiotta et al., 2016). Additionally, reefs with higher relief have displayed higher oyster abundances and greater persistence than low-relief reefs (Schulte et al., 2009; Lipcius et al., 2015; Colden et al., 2017). Vertical orientation on the reef as well as refuge are critical to the development of reef community, suggesting that these variables should be considered in monitoring and the design of restoration efforts (Soniat et al., 2004).

While the connection between intertidal oyster reef structure and condition is not as well documented as other biogenic reefs such as corals, there have been recent advances to further our understanding of the relationship. For example, there have been efforts to study the structure of intertidal oyster reefs within the context of interstitial spaces that create habitat for other species (Kim et al., 2018; Lavan, 2019), and to evaluate how the multiscale topographic signatures of intertidal oyster reefs vary from surrounding habitats (Lecours and Espriella, 2020). Additionally, Windle et al. (2022) uses spectral and structural characteristics to estimate intertidal oyster reef density using SfM photogrammetry.

Lidar-derived point clouds and DSMs offer valuable tools we can use to further our knowledge on the connection between oyster reef structure and reef condition. Intertidal oyster reef relief and vertical complexity have been studied using lidar in the past, but many of these studies used aerial lidar from occupied aircrafts, which limits the point density and consequently the resolution of the DSM (Hogan & Reidenbach, 2019). These studies allow analyzing relief at the reef scale but do not provide the details relevant for capturing vertical orientation and fine-scale structure of oysters on the reefs. Although point densities vary greatly depending on the survey design and equipped sensors, the highest topographic data quality level according to the United States Geological Survey (USGS) for aerial lidar is at least 8 points per square meter, while UAS lidar can collect hundreds of points per square meter (Resop et al., 2019; Xiao et al., 2019; USGS, 2023). Others have used a terrestrial laser scanner (Rodriguez et al., 2014; Ridge et al., 2015), which provides dense datasets but limits the extent that can be surveyed. UAS-based lidar can rapidly collect dense point clouds over relatively large areas, enabling detailed analyses of multiple intertidal oyster reefs from a dataset collected in a single flight. Quantifying vertical complexity using UAS lidar-derived DSMs also allows for continuous characterization over the reef surface.

This study aims to expand on recent advances in intertidal oyster reef surface complexity research by assessing whether geomorphometrics derived from a UAS lidar-based DSM can be used to reliably model live oyster densities. The underlying assumption, validated by the ecological literature, is that vertically oriented oysters are indicative of live oysters, and more live oysters represents a healthier reef (Grabowski, 2004; Whitman & Reidenbach, 2012). Successfully characterizing reefs using surface complexity metrics would increase the feasibility of rapid and effective intertidal oyster monitoring over greater spatial areas. This represents a critical management need because oyster declines may be sudden and possibly long-lasting (Pine et al., 2015; Moore et al., 2018; Johnson et al., 2022). Additionally, restoration actions have proven insufficient to achieve recovery and have provided limited information on why reef collapse occurred (Pine et al. 2022; La Peyre et al. 2022). More efficient monitoring might provide advance warning of declining populations and improve effective restoration monitoring.

2. Materials and methods

2.1. Study site

Data were collected at the mouth of Little Trout Creek (29°15′34.98″N, 83°4′29.68″W), Florida, USA (Fig. 1). Little Trout Creek is a tidal creek with mudflat, saltmarsh, and intertidal oyster reefs present. It is located on the southern boundary of the Lower Suwannee

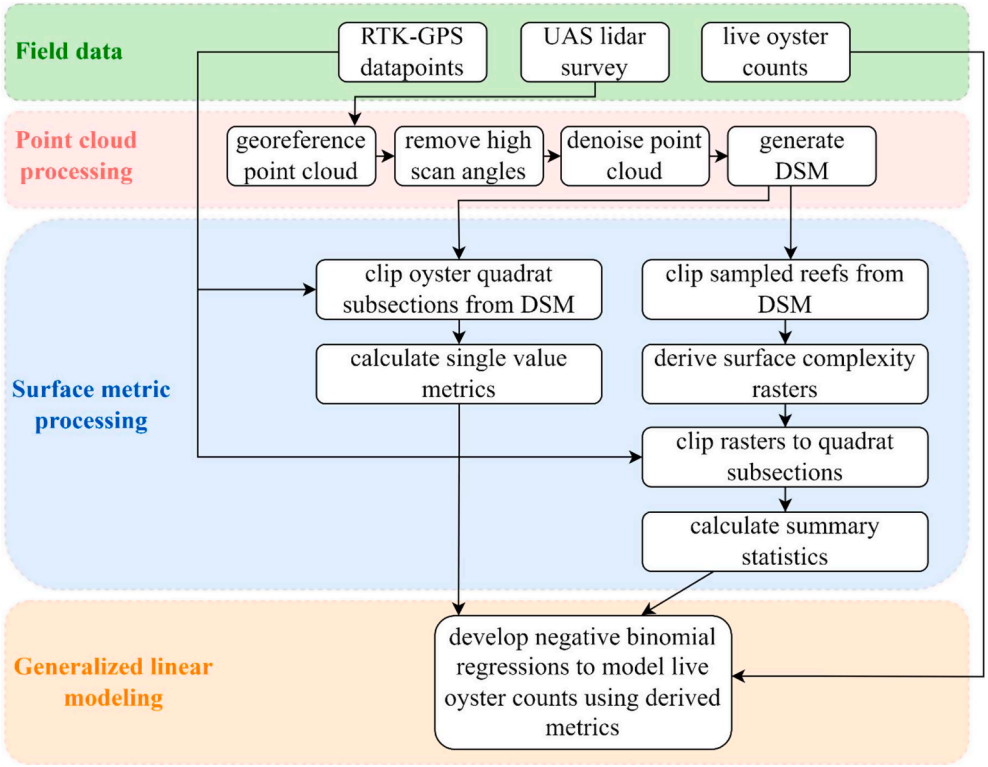

Fig. 3. Diagram highlighting the key steps in the data processing workflow.

National Wildlife Refuge within the Suwannee River estuary on Florida's Gulf of Mexico coastline. The Suwannee River estuary is part of Florida's Big Bend coastline, one of the least developed coastal areas in the United States (Main & Allen, 2007). The estuary has an average depth of 2.2 m relative to Mean Sea Level, and experiences semidiurnal tides with a tidal range of about 1 m at the mouth of the Suwannee River (Light et al., 2002; Tuckney & Dehaven, 2006; Guerra-Chanis et al., 2019). Intertidal oyster reefs occur throughout the estuary, and their orientation parallel to the coastline may aid in detaining freshwater, which maintains the brackish conditions that promote estuarine processes (Kaplan et al., 2016). Oyster reef area is declining in this region with an estimated 66% net loss from 1982 to 2011 (Seavey et al. 2011).

2.2. Survey and ground-truthing

Field observations took place on 15 February 2021 at low tide (-0.40 m relative to Mean Sea Level) to ensure maximum exposure of the oyster reefs (Cedar Key tide station ID: 8727520, NOAA Tides and Currents, 2021). Five 1-meter quadrats were placed on oyster reefs in a way to optimize their spatial distribution throughout the study area (Fig. 2). Each quadrat was equally divided into four subsections (i.e., 0.5 m × 0.5 m each), and live oysters with a length greater than 10 mm were enumerated within each section. A real-time kinematic (RTK) global navigation satellite system (GNSS) survey was conducted with a Trimble SPS986 system to record the geographical locations of the inside corners of the placed quadrats.

UAS lidar was collected over Little Trout Creek using a DJI Matrice M600 Pro equipped with a Velodyne (San Jose, California, USA) HDL-32e lidar sensor (Fig. 3). This sensor uses 32 beams and emits about 700,000 laser pulses per second with a vertical accuracy of ±2 cm. The sensor uses a near-infrared wavelength of 905 nm. Although water absorbs infrared wavelengths, near-infrared lasers have performed well when used on exposed, wet oysters (Ridge et al., 2023). The pre-programmed survey was flown at an altitude of 30 m with 50% sidelap (i.e., overlap between scanning swaths) and a 90° across-track field of view. Flying at 30 m allows for an appropriate point density for the targeted 1 cm DSM. Setting sidelap to 50% ensures 100% total overlap (excluding the outermost flightlines), limiting data gaps and shadows (Mitchell et al., 2018). The lidar scanner is part of an integrated UAS lidar mapping payload from Phoenix LiDAR Systems (Austin, Texas, USA) that includes a GNSS receiver and an inertial measurement unit (IMU). Data from these sensors, coupled with static GNSS observations from a nearby GNSS antenna, were processed as a navigation solution in Inertial Explorer® software (NovATel Inc., Canada). This navigation solution was used to directly generate a georeferenced lidar point cloud using SpatialExplorer software v6 (Phoenix LiDAR Systems). The dataset was collected in the World Geodetic System (WGS) 84 / Universal Traversal Mercator (UTM) 17 N geodetic frame of reference, and elevation was measured in reference to the WGS84 ellipsoid.

2.3. Point cloud processing

Point cloud processing was conducted using LAStools (rapidlasso GmbH, Germany), a software suite that allows for batch-scripted lidar processing (Isenburg, 2014). First, the 'las2las' command was used to write the datum projection and remove high scan angles, which have been shown to exhibit a range bias (Wallace et al., 2012). Points within −45 to 45 degrees off nadir were retained. The point cloud was then segmented into tiles using 'lastile' to make smaller files with a more manageable size. Each tile was 10 m with a 3 m buffer. Following the tiling, 'lasnoise' was used to remove points without at least 15 neighbors in a one cubic meter surrounding box. Points outside these bounds were considered noise and removed from the data. The point nearest to the 50th percentile within a cloud step size of 0.01 was kept, and the others were discarded. The 'las2dem' tool was then used to generate a DSM with a pixel size of 1 cm. The DSM was re-tiled using the same procedure as above for file size management.

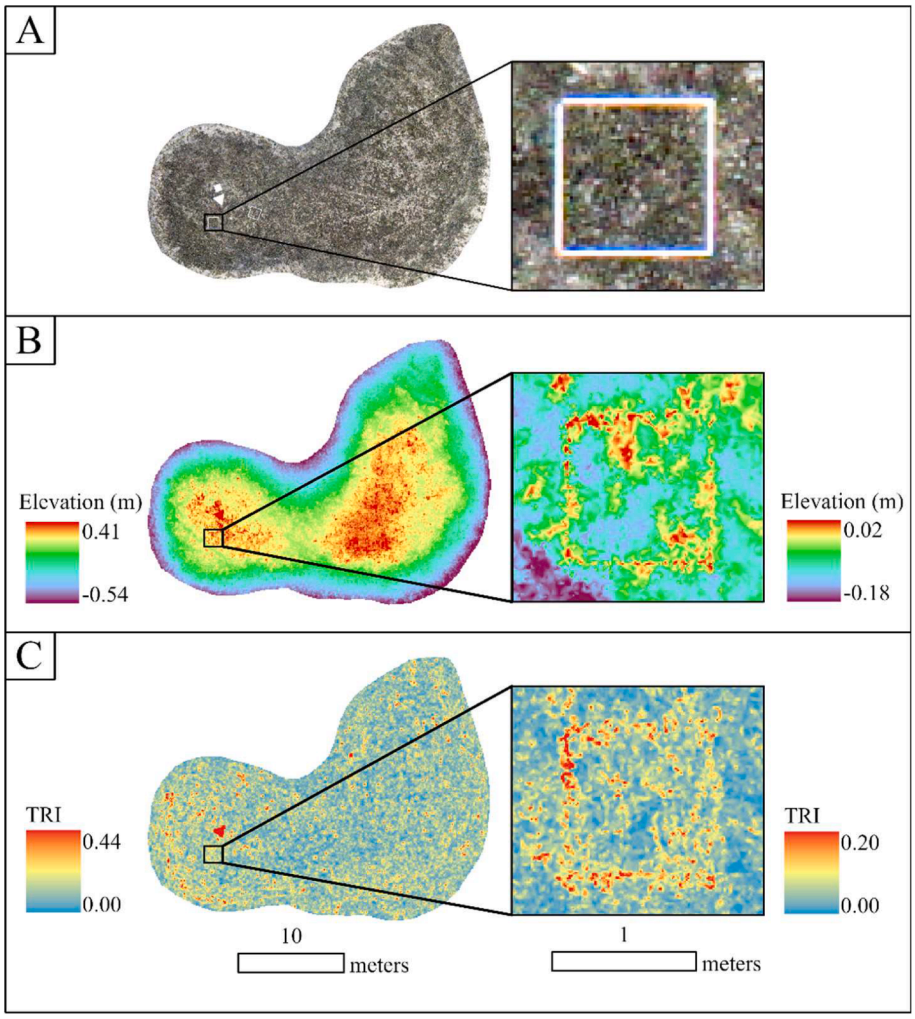

Fig. 4. (A) UAS imagery, (B) lidar-derived DSM, and (C) terrain ruggedness index (TRI) raster corresponding with an intertidal oyster reef. TRI is an example of a surface complexity metric that measures the difference in elevation between a center cell and the neighboring cells in a window. Each panel is displayed at the extent of a reef (left) and an area with a placed 1 m^2 quadrat (right). Displayed elevation values are relative to the North American Vertical Datum of 1988 (NAVD88).

2.4. Surface complexity metrics

The DSM tiles were merged using the 'Mosaic to New Raster' tool in ArcGIS Pro v2.4 (Esri® software) to produce continuous surfaces representing the intertidal oyster reefs. Polygons were manually drawn around the perimeter of each sampled reef. Then, the corresponding area in the DSM was extracted with the 'Extract by Mask' tool in ArcGIS Pro using the respective manually drawn extent polygon as the mask.

Some derived surface complexity metrics such as volume to area ratio produced a single value summarizing the area of analysis. For metrics that produced a single value, the RTK recorded quadrat corners and the midpoints between those corners were used to delineate and extract each 0.5 m × 0.5 m (0.25 m^2) quadrat subsection from the DSM. Each quadrat subsection served as a sample for a total of 20 samples across the 5 quadrats. The surface complexity metric was calculated within each of those 20 extracted areas.

Additional surface complexity metrics were calculated on a pixel-by-pixel basis, producing values across an entire DSM raster. Processing for these metrics differed slightly from those that produced a single value. These metrics produced rasters which were derived using the *geodiv*, *glcm*, *MultiscaleDTM*, *spatialEco*, *terra*, and *whitebox* packages in R v4.1 (R core team 2021). Complexity rasters were derived at the reef extent (i.e., using the DSM of the entire reef), mitigating concerns of using discrete and discontinuous habitat patches and minimizing edge effect (Fig. 4; Lecours and Espriella, 2020). Each quadrat subsection was then extracted from the surface complexity raster using RTK recorded corners and midpoints between corners, as done above.

For complexity metrics that produced rasters, the median, mean, standard deviation, skewness, and kurtosis of raster values within each quadrat subsection were calculated using the 'cellStats' function in the *raster* package in R. These values, along with the single value metrics described above, served as independent variables in the modeling workflow (Table 1). There were some exceptions, such as excluding central tendency measures for variables that are relative to the mean elevation in the window, as these would be relatively uniform with variations above and below the mean offsetting. Some of the tested metrics are multiscale and perform the operation iteratively at a range of specified scales of analysis (i.e., window sizes). The result is a raster that reports the maximum value across the specified scales at each pixel, and the scale at which that maximum value was calculated. The range of tested scales for all multiscale metrics was from 1 cell to 50 cells (the width of the quadrat subsection). A 3 × 3 window size, which resulted in an analyzed area for each pixel of 3 cm × 3 cm given the 1 cm resolution of the data, was used for all other raster-producing metrics.

Table 1
Surface complexity metrics. For metrics that produced rasters, ^ denotes measures of spread were used (i.e., standard deviation, skewness, and kurtosis), while * denotes central tendency measures were used (i.e., mean and median). Multiscale measures that indicate a $k \times k$ focal window tested analysis scales ranging from 1 cell to 50 cells.

Surface complexity metric	Description	Tool and References
3D to 2D area ratio	ratio of three-dimensional surface area to two-dimensional planar area	Surface volume (ArcGIS); Jenness (2004)
Adjusted rugosity	standard deviation of elevation, adjusted for slope by fitting a sliding window plane to the data*^	MultiscaleDTM (R); Ilich et al. (2021)
Anisotropy strength	how elevation changes considering direction; computed with median absolute differences (MAD) with kernel of order 2 and lag of 1 pixel*^	terra (R); Hijmans (2022); Trevisani & Rocca (2015); Trevisani et al. (2022)
Average roughness	average roughness of a surface calculated by the absolute deviation of elevation from the mean surface elevation	geodiv (R); McGarigal et al. (2009)
Gray level co-occurrence matrix contrast	local variations in the raster; computed with 32 gray levels, a 3 × 3 window, and 45-degree shift*^	glcm (R); Haralick et al. (1973); Hall-Beyer (2017); Zvoleff (2020)
Gray level co-occurrence matrix correlation	linear dependency of gray levels on neighboring pixels; computed with 32 gray levels, a 3 × 3 window, and 45-degree shift*^	glcm (R); Haralick et al. (1973); Hall-Beyer (2017); Zvoleff (2020)
Gray level co-occurrence matrix dissimilarity	distance between pairs of pixels; computed with 32 gray levels, a 3 × 3 window, and 45-degree shift*^	glcm (R); Haralick et al. (1973); Hall-Beyer (2017); Zvoleff (2020)
Gray level co-occurrence matrix entropy	randomness in the raster; large when the raster is not texturally uniform; computed with 32 gray levels, a 3 × 3 window, and 45-degree shift*^	glcm (R); Haralick et al. (1973); Hall-Beyer (2017); Zvoleff (2020)
Gray level co-occurrence matrix homogeneity	closeness of distribution to the GLCM diagonal; increases if larger values are on main diagonal; computed with 32 gray levels, a 3 × 3 window, and 45-degree shift*^	glcm (R); Haralick et al. (1973); Hall-Beyer (2017); Zvoleff (2020)
Gray level co-occurrence matrix mean	mean gray level values; computed with 32 gray levels, a 3 × 3 window, and 45-degree shift*^	glcm (R); Haralick et al. (1973); Hall-Beyer (2017); Zvoleff (2020)
Gray level co-occurrence matrix energy	sum of squared elements in GLCM; maximum value of 1; computed with 32 gray levels, a 3 × 3 window, and 45-degree shift*^	glcm (R); Haralick et al. (1973); Hall-Beyer (2017); Zvoleff (2020)
Gray level co-occurrence matrix variance	heterogeneity in the raster; increases when values differ from mean; computed with 32 gray levels, a 3 × 3 window, and 45-degree shift*^	glcm (R); Haralick et al. (1973); Hall-Beyer (2017); Zvoleff (2020)
Isotropic roughness	short-range isotropic (i.e., omnidirectional) roughness computed with median absolute differences (MAD); computed with kernel of order 2 and lag of 1 pixel*^	terra (R); Trevisani & Rocca (2015); Trevisani et al. (2022)
Kurtosis	a measure of the heaviness of distribution tails from DSM raster values	geodiv (R); DeCarlo (1997), Walbridge et al. (2018)
Multiscale elevation percentile	elevation percentile value furthest from 50% for each raster cell within the range of tested scales*^	Whitebox Tools (R); Lindsay (2016), Lindsay et al. (2015)
Multiscale maximum elevation deviation	multiscale measure of the maximum deviation from mean elevation*^	Whitebox Tools (R); Lindsay (2016), Lindsay et al. (2015)
Multiscale roughness	calculates surface roughness over a specified range of spatial scales*^	Whitebox Tools (R); Lindsay (2016), Lindsay et al. (2015)
Multiscale slope	allows for calculation of slope at multiple $k \times k$ focal windows; calculated using 'queen case'	MultiscaleDTM (R); Horn (1981); Ilich et al. (2021), Misiuk et al. (2021)
Multiscale standard deviation normals	maximum spherical standard deviation for each pixel across specified spatial scales*^	Whitebox Tools (R); Lindsay (2016), Lindsay et al. (2015)
Planform curvature	curvature measured as perpendicular to the direction of maximum slope^	spatialEco (R); Zevenbergen and Thorne (1987)
Profile curvature	curvature measured as direction of the maximum slope^	spatialEco (R); Zevenbergen and Thorne (1987)
Relative difference from mean value	the relative difference from mean value within a window^	MultiscaleDTM (R); Ilich et al. (2021), Lecours et al. (2017)
Skewness	asymmetry of elevation distribution; calculates Fisher-Pearson coefficient of skewness of raster values	geodiv (R); Pearson and Henrici (1895)
Standard deviation	standard deviation of DSM raster values	spatialEco (R); Walbridge et al. (2018)
Surface area ratio based on slope	estimate of surface area derived from slope and aspect of cell in raster*^	spatialEco (R); Berry (2002)
Surface area ratio	ratio of flat surface area to the digital surface model surface area	geodiv (R); McGarigal et al. (2009)
Surface area to planar area rugosity	surface area to planar area rugosity with correction of planar area for slope*^	MultiscaleDTM (R); Ilich et al. (2021), Jenness (2004), Du Preez (2015)
Surface relief ratio	difference between the mean and minimum elevation in a window, divided by the range^	spatialEco (R); Pike and Wilson (1971)
Terrain ruggedness index	elevation difference between adjacent cells in raster*^	spatialEco (R); Riley et al. (1999)
Topographic position index	a measure of a cell's elevation variation compared to its neighbors in a focal window^	spatialEco (R); De Reu et al. (2014)
Vector ruggedness measure	variation in three-dimensional orientation of cells within a window*^	spatialEco (R); Sappington et al. (2007)
Volume to area ratio	volume of raster divided by area of raster; the lowest elevation in the respective extracted DSM area served as the baseline plane for calculating volume	Surface volume (ArcGIS); Yanalak and Baykal (2003)

2.5. Modeling of relationships between live oyster counts and surface complexity

Our modeling approach had two steps: we first predicted oyster counts with single surface complexity metrics individually, and then used the results to reduce the number of surface complexity metrics considered for multi-predictor candidate models. To model live oyster counts in relation to individual surface complexity metrics, we used negative binomial generalized linear models (GLM). Negative binomial models were selected because they are appropriate for modeling count data when the distribution exhibits overdispersion (i.e., the count variance is greater than the mean), as seen with our oyster count data (Jain & Consul, 1971; Moore et al., 2020). Models were developed using the 'glm.nb' function within the *MASS* package in R (Venables & Ripley, 2002). Each of the complexity metrics was used as an individual independent variable in a negative binomial GLM. This permitted for the comparison of each independent variable as the sole predictor for the response metric (live oyster counts). Models were sorted using Akaike information criteria (AIC) corrected for small sample size (AICc) to compare model fits, where a lower AICc indicates a better fit. AIC has the potential to overfit when the sample size is small, therefore, AICc was used; Burnham et al. (2002) recommend using the bias corrected AICc rather than AIC when the ratio of sample size to total number of parameters is less than 40.

Only those independent variables (i.e., surface complexity metrics) that were found to have statistically significant relationships in individual models were retained to determine if including multiple complexity metrics improved the model. First, a Spearman correlation

Table 2
Models that produced significant relationships with live oyster counts, ranked by corrected Akaike information criterion adjusted for small sample size (AICc). SE refers to standard error, and Pr(<z) reports the p-value.

		Intercept			Parameter		
Parameter	**AICc**	**Estimate**	**SE**	**Pr(>z)**	**Estimate**	**SE**	**Pr(>z)**
Median of GLCM variance	172.39	2.81	0.18	<0.01	0.003	0.001	<0.01
Median of GLCM mean	172.90	2.14	0.30	<0.01	2.91	0.56	<0.01
Mean of GLCM variance	172.93	2.77	0.19	<0.01	0.003	0.001	<0.01
Skewness of GLCM variance	173.05	4.41	0.18	<0.01	−0.98	0.18	<0.01
Mean of GLCM mean	173.64	2.09	0.32	<0.01	2.95	0.59	<0.01
Standard deviation of GLCM contrast	174.16	4.57	0.21	<0.01	−0.40	0.08	<0.01
Kurtosis of GLCM variance	174.51	3.26	0.13	<0.01	−0.51	0.10	<0.01
Volume to area ratio	174.59	2.11	0.32	<0.01	31.27	6.23	<0.01
Skewness of elevation	174.62	4.20	0.16	<0.01	−2.09	0.40	<0.01
Standard deviation of GLCM dissimilarity	174.98	5.52	0.38	<0.01	−3.22	0.62	<0.01
Standard deviation of GLCM correlation	175.81	2.87	0.21	<0.01	0.64	0.15	<0.01
Skewness of multiscale max elevation deviation	176.92	4.09	0.15	<0.01	−1.57	0.32	<0.01
Skewness of GLCM mean	178.64	4.15	0.17	<0.01	−1.17	0.26	<0.01
Kurtosis of elevation	178.67	2.62	0.28	<0.01	−0.87	0.21	<0.01
Standard deviation of GLCM homogeneity	179.02	8.82	1.14	<0.01	−28.38	6.23	<0.01
Mean of GLCM contrast	179.38	4.52	0.24	<0.01	−0.48	0.12	<0.01
Kurtosis of GLCM mean	179.81	2.49	0.31	<0.01	−0.95	0.24	<0.01
Kurtosis of multiscale max elevation deviation	180.65	0.84	0.78	<0.01	−1.63	0.45	<0.01
Mean of GLCM dissimilarity	181.15	5.07	0.41	<0.01	−1.63	0.44	<0.01
Mean of GLCM homogeneity	182.40	0.25	1.02	0.80	5.28	1.57	<0.01
Mean of GLCM entropy	182.67	6.34	0.83	<0.01	−1.87	0.57	<0.01
Median of GLCM energy	182.73	2.01	0.52	<0.01	6.38	1.95	<0.01
Median of multiscale max elevation deviation	182.82	3.80	0.14	<0.01	0.78	0.24	<0.01
Median of multiscale elevation percentile	182.88	2.75	0.31	<0.01	0.02	0.01	<0.01
Median of GLCM homogeneity	183.01	0.78	0.92	0.40	4.37	1.38	<0.01
Mean of GLCM energy	183.22	1.91	0.56	<0.01	5.81	1.80	<0.01
Median of GLCM entropy	183.68	6.03	0.79	<0.01	−1.60	0.53	<0.01
Skewness of surface relief ratio	184.41	3.50	0.15	<0.01	−3.78	1.25	<0.01
Skewness of GLCM energy	184.72	5.14	0.56	<0.01	−0.75	0.28	0.01
Median of GLCM dissimilarity	184.77	4.88	0.44	<0.01	−1.63	0.57	<0.01
Median of GLCM contrast	185.42	4.33	0.29	<0.01	−0.64	0.24	0.01
Mean of GLCM correlation	185.65	1.28	0.89	0.15	4.98	1.81	0.01
Skewness of GLCM entropy	185.92	4.43	0.35	<0.01	1.07	0.46	0.02
Skewness of multiscale elevation percentile	186.12	3.91	0.17	<0.01	−1.11	0.44	0.01
Mean of multiscale elevation percentile	186.38	1.28	0.97	<0.01	0.05	0.02	0.01
Surface area ratio	186.43	4.54	0.38	<0.01	−2.21	0.90	0.01
Standard deviation of relative deviation from mean value	186.45	7.76	1.45	<0.01	–23.01	8.16	<0.01
Standard deviation of GLCM energy	186.55	2.10	0.65	<0.01	9.60	3.85	0.01
Standard deviation of elevation	186.63	2.24	0.64	<0.01	67.44	28.89	0.02
Skewness of GLCM homogeneity	186.64	3.32	0.23	<0.01	−1.31	0.61	0.03
Kurtosis of vector ruggedness measure	187.08	4.08	0.23	<0.01	−0.201	0.09	0.03
Mean of multiscale max elevation deviation	188.01	3.69	0.15	<0.01	1.30	0.65	0.04
Skewness of anisotropy strength	188.04	4.12	0.25	<0.01	−0.62	0.31	0.04
Standard deviation of multiscale standard deviation normals	188.10	5.66	0.88	<0.01	−0.26	0.12	0.02
Kurtosis of isotropic roughness	188.30	4.08	0.23	<0.01	−0.15	0.07	0.04
Kurtosis of anisotropy strength	188.55	3.81	0.16	<0.01	−0.08	0.04	0.04

matrix was made to identify independent variables that were highly correlated (|r| greater than 0.7) (Dormann et al., 2013). Independent variables correlated with the highest number of other independent variables were removed first. Once only single pairs of correlated independent variables remained, the independent variable with the higher AICc was removed. The remaining independent variables were then used to construct a series of candidate models that could be subjected to a model selection procedure. The 'dredge' function from the *MuMIn* package in R was used to produce the best performing negative binomial GLMs, as ranked by AICc (Bartón, 2022). The 'dredge' function produces a model selection table, reporting performance metrics such as AICc for each combination of independent variables. A maximum of two independent variables were allowed in these candidate models to mitigate concerns of overfitting, given the small sample size (Hair et al., 2010).

3. Results

3.1. Oyster counts and surface complexity metrics

Live oyster density over 10 mm ranged from 9 to 156 individuals per 0.25 m^2 quadrat subsection (mean 42.1, median 34, standard deviation 35). A single observer took approximately 12 min to enumerate oysters per 1 m^2.

A total of 122 independent variables for the modeling were derived from the surface complexity metrics, including three summary statistics from the DSM, four metrics that produced a single value for the quadrat subsection, and 115 summary statistics representing 25 surface complexity rasters (see Supplementary Material).

3.2. Single predictor models

Of the 122 independent variables tested, 46 produced models with statistically significant relationships ($p \leq 0.05$) for the independent variable. Measures of spread (i.e., standard deviation, skewness, kurtosis) characterizing the DSM all produced significant models. Of the 40 independent variables representing gray level co-occurrence matrix (GLCM) measures, 27 produced models with statistically significant relationships for the independent variable. The median of GLCM variance produced the model with the lowest AICc, and the top seven models ranked by AICc are GLCM features (Table 2).

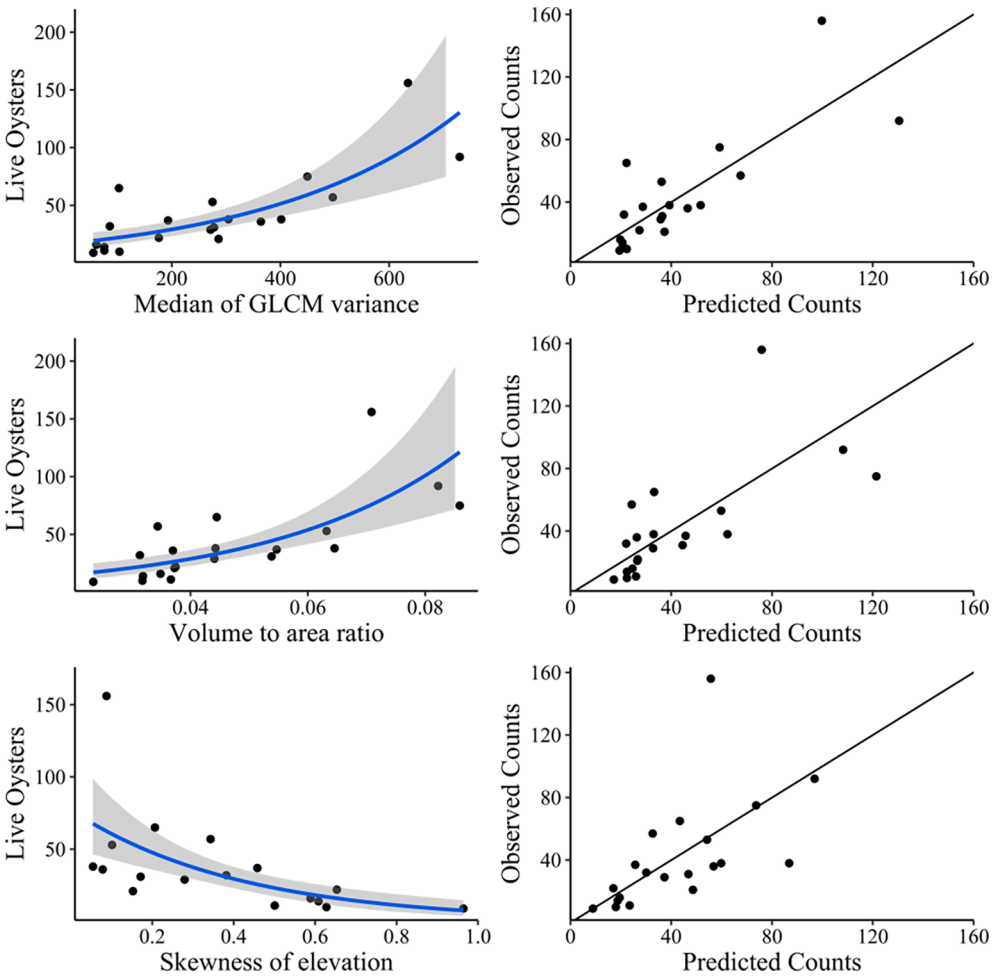

Fig. 5. Three models (left panel) representing the best performing raster metric (median of GLCM variance), single-value metric (volume to area ratio), and DSM summary statistic (skewness of elevation). The blue line represents the regression line, and the grey shading represents the 95% confidence interval. The comparison of observed counts to predicted counts for each respective model is displayed to the right. A line with a slope of one on the right panels is depicted to represent perfect agreement. (For interpretation of the references to colour in this figure legend, the reader is referred to the web version of this article.)

Volume to area ratio was the best performing 'single-value' metric, as ranked by AICc. This metric represents vertical complexity by quantifying the amount of shell present per unit area and has the potential to inform shell budget (the rate of shell deposition compared to rate of shell loss) estimations above the plane represented by the reef surface (i.e., substrate or shell hash).

Every model underestimated the highest count of 156, performing better with low and medium counts (Fig. 5). Removing the outlier of 156 improved every significant model, reducing AICc by an average of 15.9. However, this count was ultimately included in the models to capture the significant variability displayed in live oyster densities over the span of a reef.

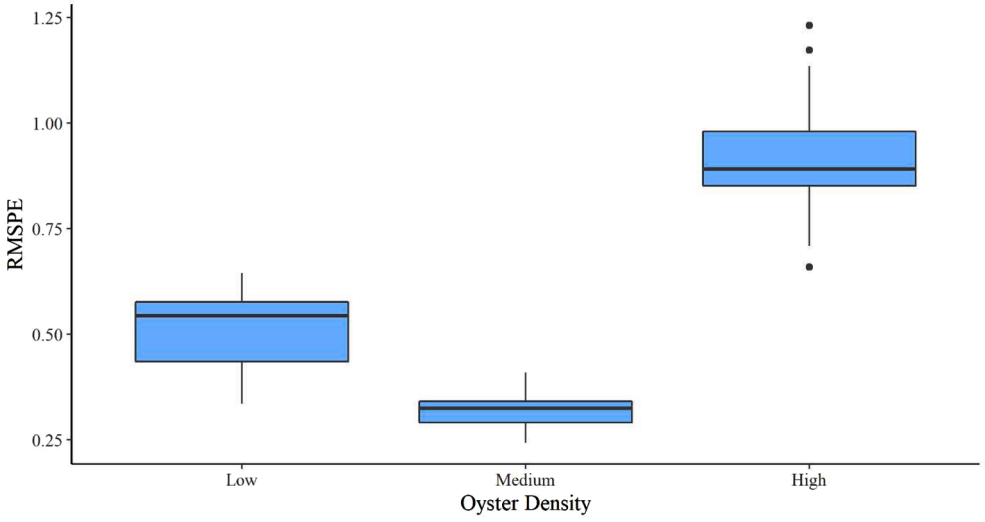

Fig. 6. Average root mean square percent error (RMSPE) across the 46 significant models for low (9–22/0.25 m^2), medium (29–38/0.25 m^2), and high (53–156/0.25 m^2) oyster densities.

Table 3
Top six models generated from the model selection procedure. AICc refers to Akaike Information Criterion adjusted for small sample size, SE refers to standard error, and Pr(<z) reports the p-value.

Parameters	AICc	Intercept		Parameter 1		Parameter 2	
		Estimate ± SE	Pr (>z)	Estimate ± SE	Pr (>z)	Estimate ± SE	Pr (>z)
Volume to area ratio + standard deviation of GLCM homogeneity	167.30	5.55 ± 0.96	<0.01	26.23 ± 5.08	<0.01	−17.72 ± 4.64	<0.01
Volume to area ratio + standard deviation of standard deviation normals	167.76	4.06 ± 0.56	<0.01	31.58 ± 4.87	<0.01	−0.27 ± 0.07	<0.01
Median of GLCM variance + standard deviation of GLCM homogeneity	170.50	5.69 ± 1.06	<0.01	0.002 ± 0.001	<0.01	−14.91 ± 5.32	0.01
Median of GLCM variance + skewness of anisotropy strength	172.01	3.12 ± 0.21	<0.01	0.003 ± 0.0005	<0.01	−0.48 ± 0.20	0.02
Standard deviation of GLCM correlation + standard deviation of GLCM homogeneity	172.89	6.14 ± 1.03	<0.01	0.48 ± 0.14	<0.01	−17.08 ± 5.21	<0.01
Median of GLCM variance + volume to area ratio	172.89	2.29 ± 0.28	<0.01	0.002 ± 0.0007	0.01	16.61 ± 7.91	0.04

Root mean square percent error (RMSPE) was calculated for each of the 46 significant models. Densities were categorized into thirds (i.e., low, medium, high) to assess the models' performance; the seven lowest densities (9–22/0.25 m^2), middle seven densities (29–38/0.25 m^2), and six highest densities (53–156/0.25 m^2) were grouped to analyze average RMSPE in each category. The predicted counts from the models differed from observed counts the most in areas of high density and the least in areas of medium density (Fig. 6). The overall average RMSPE was 0.62. The standard deviation of GLCM homogeneity model produced the lowest RMSPE of 0.51 for the models with a single independent variable.

3.3. Multi-predictor models

Following the correlation analysis, 12 surface complexity metrics remained: kurtosis of GLCM mean, kurtosis of isotropic roughness, kurtosis of vector ruggedness measure, median of GLCM variance, standard deviation of GLCM correlation, standard deviation of GLCM homogeneity, skewness of anisotropy strength, skewness of multiscale elevation percentile, skewness of surface relief ratio, standard deviation of standard deviation normals, surface area ratio, and volume to area ratio (Appendix A). The top four models allowing for multiple independent variables produced lower AICc values than the best performing model with a single independent variable (median of GLCM variance). Additionally, the top six multi-predictor models (Table 3) were significantly different from their respective single-predictor counterparts, as indicated by ANOVA. The average RMPSE for these six multi-predictor models was 0.43 with a low of 0.37 for the model that included volume to area ratio and the standard deviation of GLCM homogeneity.

4. Discussion

4.1. Surface complexity metric performance

This study builds on the growing literature using UAS to study intertidal oyster reefs and provides insight on which surface complexity metrics may offer the best indicator for reef condition. Promising results indicate that surface complexity metrics may provide valuable information on reef condition. GLCM textural metrics produced 27 of the 46 significant single-predictor models, and at least one GLCM measure was included in five of the six best multiple-predictor models. A GLCM is created from a gray-scale image and represents the distribution of co-occurring values in a specified spatial relationship (Haralick et al., 1973; Hall-Beyer, 2017). Although GLCM metrics are most frequently applied to spectral images, applications to digital elevation model data are increasing, largely within the scope of landform segmentation and classification (Liu et al., 2017; Zhu et al., 2019). GLCM metrics are used to identify local patterns in an image and excelled at producing patterns that predicted live intertidal oyster counts in this study. While GLCM metrics performed well, other high-performing variables such as volume to area ratio may have a more direct parallel to ecological processes at scale. The volume to area ratio rather than volume was primarily used to account for small variations in the size of the delineated 0.25 m^2 sample area, but also carries the additional advantage of being more transferable to larger areas of interest. The positive relationship between volume to area ratio and live intertidal oyster counts indicates that areas with high relief may coincide with more live oysters and, therefore, a well-conditioned reef. The ratio has the potential to identify areas that have oyster clusters, a dominant feature on intertidal reefs in Florida (Tolley & Volety, 2005). Oyster clusters represent a valuable feature to characterize structurally, given their habitat value and provision of settlement substrate (Tolley & Volety, 2005; Wilberg et al., 2013). Volume to area ratio can also inform management or restoration efforts on shell budget targets. Oyster reefs that maintain a balanced shell budget are more resilient to stressors such as sea level rise (Radabaugh et al., 2019). Monitoring shell budget over wide extents using UAS surveys can provide valuable information on reef resiliency in a changing climate.

Measures of spread (i.e., skewness, kurtosis, and standard deviation) characterizing the elevation data from the DSM all produced significant models. These parameters require no additional processing following the derivation of the DSM, further simplifying the workflow. Skewness was the best performing summary statistic, as indicated by AICc. The negative relationship between skewness and live oyster counts suggests that areas with a higher concentration of relatively high elevation shells host more live oysters. A negative skewness occurs when the tail of the distribution is longer on the left side, meaning that the presence of live oysters is associated with few raster cells at a low elevation but many cells at a higher elevation, which may align with the presence of oyster clusters.

The high performance of multiscale measures suggests that a single scale may be insufficient to study intertidal oyster reef structure and complexity. The DSM derived from the point cloud had a resolution of 1 cm, and single-scale metrics that used windows to calculate variation (e.g., terrain ruggedness index) used 3 × 3 windows. Multiscale measures considered all scales to the extent of the relevant quadrat subsection (i.e., up to 50 × 50). Multiscale metrics mitigate the shortcomings of arbitrarily selecting a scale of analysis (Lecours et al., 2015; Misiuk et al., 2018). Lecours and Espriella (2020) used the 'multiscale roughness' tool (Lindsay, 2016) at the reef scale (i.e., allowing for analysis scales up to the length of the reef) and found that the highest magnitude

of roughness for intertidal oysters was displayed at a median scale of about 5.3 m. Should the presented method be applied at the scale of an entire reef, the scale of analysis should be carefully considered, and multiscale approaches have the potential to better capture reef geomorphometry at varying scales (Ilich et al., 2021; Misiuk et al., 2021). The maximum scale considered for multiscale metrics was set to 50 raster cells to coincide with the extent of the quadrat subsection and capture variability at the same scale in which oyster counts were observed. Each multiscale feature from Whitebox Tools also produces a raster indicating at which scale the maximum value was produced for each cell. Histograms of these raster values were visually examined to ensure that the values were not clustered at or near 50, which could suggest that the optimal scale for capturing the variable of interest may be beyond 50. The scale values were well distributed, limiting this concern. However, the maximum scale should be adjusted accordingly for applications at the reef scale, and with the scale of observation. While multiscale approaches lessen concerns about arbitrary selection, it is still necessary to consider the ecological process or pattern of interest when selecting parameters such as maximum scale (Lecours et al., 2015). Future work will look to further implement multiscale approaches as the workflow is applied beyond a specified quadrat dimension.

Six multi-predictor models were able to better predict live oyster counts than single predictor models, as indicated by AICc and RMSPE. The complexity of candidate models was limited by the small sample size, however the multi-predictor models demonstrated promising results. Volume to area ratio and the standard deviation of GLCM homogeneity produced the model with the lowest AICc. The combination of these variables allows for the inclusion of structural and textural information in the model.

Model predictions demonstrated the lowest error for medium densities. While further exploration and sampling is needed to understand the weaker performance of low and high densities, it may also be appropriate to consider developing separate models by category. Error may be higher for lower densities because the surface complexity metrics are capturing variation on the substrate (i.e., shell hash). Increased sampling density will also likely improve the models, especially for high counts, which covered a large range.

4.2. Limitations and considerations

While this study serves largely as a proof-of-concept, there were notable limitations that make it essential that the results be set in context. The most notable limitation is the small sample size of the study. The study only used a total of 5 m^2 of reef area, however the results are promising and encourage further exploration of the relationship between surface complexity and intertidal oyster reef condition. Additionally, despite being from four different reef patches, all the samples are from the same survey location of Little Trout Creek. It is possible that these relationships differ in significance or magnitude at other locations in the Big Bend region, given differences in environmental conditions such as wave exposure. All the surveyed reefs are natural reefs; therefore, these findings cannot be extended to restored reefs without further exploration.

Another consideration is the selection of survey parameters. The flying height of 30 m and 50% overlap allowed for the 9.7-hectare area of interest to be surveyed in 17 min (0.57 ha/min). This coverage will vary by equipment and survey design, as well as weather conditions. While the intention of this survey was to capture very-high resolution data to capture fine-scale variation, the high performance of multiscale measures indicates that coarser resolutions may be sufficient to capture relationships between surface complexity and reef condition. Reducing the targeted point density of the lidar survey will allow for more coverage in a single flight. Surveys should be designed in line with specific objectives, while considering the appropriate scale to address those objectives.

The density and growth behavior of oysters in the area of interest should be considered within the context of this workflow. Although *Crassostrea virginica* in Florida, USA typically grow vertically in the intertidal, other oyster species can display differing growth patterns. For example, *Crassostrea gigas* demonstrates horizontal growth patterns in rocky areas on the Atlantic coast of France (Barillé et al., 2017). The relationship between surface complexity metrics and live oyster densities or reef condition will vary given the growth pattern. The mean oyster density (enumerating oysters larger than 10 mm) in the surveyed quadrats was 168/m^2. This density aligns with other studies of the Suwannee River estuary. Bergquist et al. (2006) reported counts of 34 to 411 oysters/m^2 in the Suwannee River estuary, depending on the size and location of the reef. Seavey et al. (2011) found oyster densities of about 40–50 oysters/m^2 at inshore sites within the region. However, oyster counts can vary significantly by region and by counting method (Byers et al., 2015). For example, Windle et al. (2022) excavated quadrats to a depth of 15 cm and counted all oysters to find densities as high as 6,975/m^2 on intertidal eastern oyster reefs in North Carolina, USA. This disparity emphasizes the importance of only considering these relationships within the systems that the models were built in, as well as considering survey methods. Given the surface complexity metrics derived only account for features on the surface of the reef, excavation was not considered to count oysters.

Significantly different intertidal oyster densities are likely to produce different relationships with surface complexity metrics. For example, skewness may have a different relationship to intertidal oyster counts in areas with higher densities, as there may not be as significant of an elevation disparity if the base (e.g., shell hash) of the reef is occluded by vertically oriented oysters. Additionally, including other *in situ* metrics such as oyster sizes may improve the workflow by providing information on population structure. An area with a high density of small, live oysters as opposed to an area with medium density, but large, vertically oriented oysters will produce different responses in terms of surface complexity. Therefore, it is important to consider the limitations of live counts and interpret the results of this study within context. In the present study, counts ranged from 9 to 156 per 0.25 m^2 area, but 14 of the 20 observations were below 40 and 156 was a statistical (but not ecological) outlier, thus influencing model fit. Additional sampling will provide a more continuous depiction of oyster densities, and potentially reduce the error associated with the 'high' oyster counts in the models (Fig. 6).

A generalized linear model approach was selected due to the relative simplicity of implementation and the ability to assess and visualize relationships between specific variables. However, other modeling approaches, including non-linear algorithms, may also be suited to address the same objectives. For predictive purposes, it may be appropriate to explore machine learning approaches. Windle et al. (2022) also used generalized additive models when studying reef complexity in the context of intertidal oyster densities.

4.3. Future work

The primary objective of future work should be to collect more data from different survey sites and with reefs presenting a range of oyster densities in order to develop a more robust relationship between intertidal oyster reef condition and surface complexity metrics. We also intend to explore the utility of DSMs derived from SfM photogrammetry with this workflow. A DSM and orthomosaic were developed using SfM

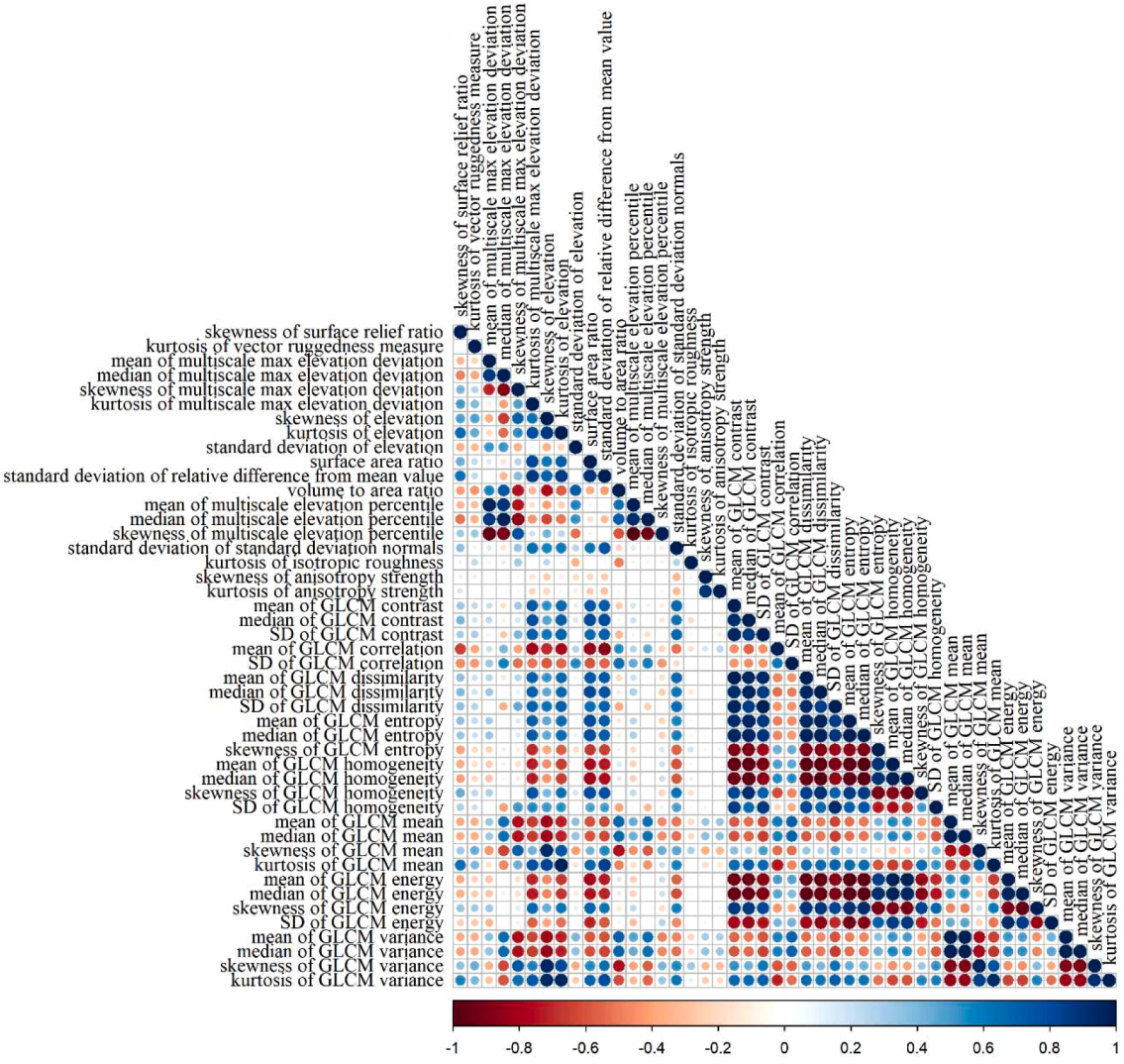

Fig. A1. Correlation matrix for the independent variables that produced significant models. SD refers to standard deviation.

photogrammetry from a flight immediately following the collection of the lidar point cloud. However, the presence of the quadrats created artifacts within the SfM-derived DSM that were difficult to reconcile without removing data within the quadrat. These artifacts could be in part due to shadows created by the quadrats, as areas obscured by shadows make it challenging to perform key point matching using image textures (James & Robson, 2012). Since they are from an active sensor, the lidar data did not present these artifacts. When collecting RTK-GPS data points to locate quadrat corners, future applications of this workflow should remove the quadrats prior to the UAS survey to minimize their influence on the structure of the reef within the area of interest. The ability to successfully apply these methods using SfM photogrammetry would make the workflow more accessible, as lidar systems can be cost-prohibitive to obtain. Further exploration is necessary to explore the trade-offs between lidar and SfM derived complexity metrics as well as their ability to represent reef condition. Although lidar systems can be cost-prohibitive, lidar data continues to become more accessible via repositories such as gulf3D.org, where surveys can be uploaded for public use.

Topographic complexity can also be used to study relationships beyond oyster densities. For example, reef status can be studied through the lens of species richness and density to quantify habitat provision (Bergquist et al., 2006). Studies have quantified oyster reef interstitial spaces and how they contribute to habitat availability (e.g., Kim et al., 2018), but there is limited understanding of how topographic complexity metrics connect to community assemblages and species densities on oyster reefs.

5. Conclusion

Understanding the structural complexity of intertidal oyster reefs is critical to their conservation and restoration. UAS provide a platform to rapidly collect information on multiple reefs in one survey by producing DSMs from which high-resolution elevation datasets can be produced. The workflow presented highlights the potential of UAS lidar-derived DSMs to produce surface complexity metrics as indicators for intertidal oyster reef condition. Should a monitoring or management organization be interested in adopting this workflow, we recommend first surveying an area of interest with lidar. Then, use the lidar point cloud to develop a DSM representing elevation over the intertidal oyster reefs. From the DSM, surface complexity metrics can be derived. Although numerous metrics produced significant relationships with live oyster counts, managers should prioritize metrics that are interpretable and relevant to objectives. For example, volume to area ratio demonstrated a significant relationship with live oyster counts and can inform shell budgets. Volume to area ratio can be derived from the DSM using tools in a GIS software such as the ‘Surface Volume’ tool in ArcGIS or calculated in R. Volume to area ratio can then be used to estimate live oyster counts

using GLMs or used directly to assess relative reef condition. Frequent monitoring of surface complexity metrics will help identify reefs exhibiting signs of worsening condition, allowing for more proactive management. Furthering our knowledge of those topographic signatures associated with reef condition will also enable restoration efforts to mimic those signatures. Additionally, metrics derived can be used to explore linkages between oyster reef surface morphology and fish and invertebrate biodiversity, as has been done with coral reefs. Restoring and preserving oyster reefs goes beyond maintaining oyster populations as reefs provide habitat for a variety of species and promote coastal resilience.

CRediT authorship contribution statement

Michael C. Espriella: Conceptualization, Methodology, Formal analysis, Writing – original draft, Visualization. **Vincent Lecours:** Conceptualization, Methodology, Writing – review & editing, Project administration, Funding acquisition. **Edward V. Camp:** Conceptualization, Methodology, Writing – review & editing. **H. Andrew Lassiter:** Conceptualization, Data curation, Resources. **Benjamin Wilkinson:** Conceptualization, Funding acquisition, Resources, Writing – review & editing. **Peter C. Frederick:** Conceptualization, Writing – review & editing. **Simon J. Pittman:** Conceptualization, Writing – review & editing.

Declaration of Competing Interest

The authors declare that they have no known competing financial interests or personal relationships that could have appeared to influence the work reported in this paper.

Data availability

Data will be made available on request.

Acknowledgements

This work was supported by the USDA National Institute of Food and Agriculture (Hatch. project FLA-FOR-005981; multiscale analysis of oyster resources using geomorphometry and remote sensing technologies), by funds allocated to V.L. by the University of Florida Senior Vice President for Agriculture and Natural Resources, and by an Early-Career Research Fellowship to V.L. from the Gulf Research Program of the National Academies of Sciences, Engineering, and Medicine. This study also was supported by the United States Department of Commerce, National Oceanic and Atmospheric Administration (NOAA), through the University of Southern Mississippi under the terms of Agreement No. NA18NOS400198. Additional support was provided by Cynthia A. Melnick Endowment. Thanks are also due to Connor Bass, Bradley Ennis, Carter Kelly, Audrey Jordan, and Natalie Stephens for assistance with fieldwork.

Appendix A

Appendix B. Supplementary data

Supplementary data to this article can be found online at https://doi.org/10.1016/j.ecolind.2023.110190.

References

Baggett, L.P., Powers, S.P., Brumbaugh, R.D., Coen, L.D., DeAngelis, B.M., Greene, J.K., Hancock, B.T., Morlock, S.M., Allen, B.L., Breitburg, D.L., et al., 2015. Guidelines for evaluating performance of oyster habitat restoration: Evaluating performance of oyster restoration. Restor. Ecol. 23, 737–745. https://doi.org/10.1111/rec.12262.

Barillé, L., Le Bris, A., Méléder, V., Launeau, P., Robin, M., Louvrou, I., Ribeiro, L., 2017. Photosynthetic epibionts and endobionts of pacific oyster shells from oyster reefs in rocky versus mudflat shores. PLoS One 12, e0185187.

Bartón, K., 2022. MuMIn: Multi-model inference. R package version 1.7. 2. *http://CRAN. R-project. org/package= MuMIn.*

Baxter, P.W.J., Hamilton, G., 2018. Learning to fly: Integrating spatial ecology with unmanned aerial vehicle Surveys. Ecosphere 9, e02194.

Beck, M.W., Brumbaugh, R.D., Airoldi, L., Carranza, A., Coen, L.D., Crawford, C., Defeo, O., Edgar, G.J., Hancock, B., Kay, M.C., Lenihan, H.S., Luckenbach, M.W., Toropova, C.L., Zhang, G., Guo, X., 2011. Oyster reefs at risk and recommendations for conservation, restoration, and management. Bioscience 61, 107–116.

Bergquist, D.C., Hale, J.A., Baker, P., Baker, S.M., 2006. Development of ecosystem indicators for the suwannee river estuary: Oyster reef habitat quality along a salinity gradient. Estuaries Coasts: J ERF 29, 353–360.

Berry, J.K., 2002. Use surface area for realistic calculations. Geoworld 15 (9), 20–21.

Brunier, G., Oiry, S., Gruet, Y., Dubois, S.F., Barillé, L., 2022. Topographic analysis of intertidal polychaete reefs (Sabellaria Alveolata) at a very high spatial resolution. Remote Sens. (Basel) 14, 307. https://doi.org/10.3390/rs14020307.

Burnham, K.P., Anderson, D.R., Burnham, K.P., 2002. Model selection and multi-model inference: A practical information-theoretic approach. Springer.

Burns, J., Delparte, D., Gates, R., Takabayashi, M., 2015. Integrating structure-from-motion photogrammetry with geospatial software as a novel technique for quantifying 3D ecological characteristics of coral reefs. PeerJ 3, e1077.

Byers, J.E., Grabowski, J.H., Piehler, M.F., Hughes, A.R., Weiskel, H.W., Malek, J.C., Kimbro, D.L., 2015. Geographic variation in intertidal oyster reef properties and the influence of tidal prism: Biogeography of intertidal oyster reefs. Limnol. Oceanogr. 60, 1051–1063. https://doi.org/10.1002/lno.10073.

J.L. Carrivick M.W. Smith Fluvial and Aquatic Applications of Structure from Motion Photogrammetry and Unmanned Aerial Vehicle/Drone Technology. WIREs Water 6 2019 doi:10.1002/wat2.1328.

Chand, S., Bollard, B., 2021. Low altitude spatial assessment and monitoring of intertidal seagrass meadows beyond the visible spectrum using a remotely piloted aircraft system. Estuarine, Coastal Shelf Science 255.

Chowdhury, M.S.N., Walles, B., Sharifuzzaman, S., Shahadat Hossain, M., Ysebaert, T., Smaal, A.C., 2019. Oyster breakwater reefs promote adjacent mudflat stability and salt marsh growth in a monsoon dominated subtropical coast. Sci. Rep. 9, 8549. https://doi.org/10.1038/s41598-019-44925-6.

Coen, L.D., Brumbaugh, R.D., Bushek, D., Grizzle, R., Luckenback, M.W., Posey, M.H., Powers, S.P., Tolley, S.G., 2007. Ecosystem services related to oyster restoration. Mar. Ecol. Prog. Ser. 341, 303–307.

Colden, A., Latour, R., Lipcius, R., 2017. Reef height drives threshold dynamics of restored oyster reefs. Mar. Ecol. Prog. Ser. 582, 1–13.

Collin, A., Dubois, S., Ramambason, C., Etienne, S., 2018. Very high-resolution mapping of emerging biogenic reefs using airborne optical imagery and neural network: The honeycomb worm (*Sabellaria Alveolata*) case study. Int. J. Remote Sens. 39, 5660–5675. https://doi.org/10.1080/01431161.2018.1484964.

De Reu, J., Bourgeois, J., Bats, M., Zwertvaegher, A., Gelorini, V., 2014. Application of the topographic position index to heterogeneous landscapes. Geomorphology 186, 39–49.

DeCarlo, L.T., 1997. On the meaning and use of kurtosis. Psychol. Methods 2, 292–307.

Dormann, C.F., Elith, J., Bacher, S., Buchmann, C., Carl, G., Carré, G., Marquéz, J.R.G., Gruber, B., Lafourcade, B., Leitão, P.J., et al., 2013. Collinearity: A review of methods to deal with it and a simulation study evaluating their performance. Ecography 36, 27–46.

Du Preez, C., 2015. A new arc-chord ratio (ACR) rugosity index for quantifying three-dimensional landscape structural complexity. Landsc. Ecol. 30, 181–192.

Dunn, D.C., Halpin, P.N., 2009. Rugosity-based regional modeling of hard-bottom habitat. Mar. Ecol. Prog. Ser. 377, 1–11.

Dustan, P., Doherty, O., Pardede, S., 2013. Digital reef rugosity estimates coral reef habitat complexity. PLoS One 8, e57386.

Espriella, M.C., Lecours, V., 2022. Optimizing the scale of observation for intertidal habitat classification through multiscale analysis. Drones 6, 140.

Espriella, M.C., Lecours, V.C., Frederick, P.V., Camp, E., Wilkinson, B., 2020. Quantifying intertidal habitat relative coverage in a florida estuary using UAS imagery and GEOBIA. Remote Sens. (Basel) 12, 677.

Florinsky, I.V., 2017. An illustrated introduction to general geomorphometry. Progress Phys. Geography: Earth Environ. 41, 723–752. https://doi.org/10.1177/0309133317733667.

Frederick, P.C., Vitale, N., Pine III, W.E., Seavey, J.R., 2016. Reversing a rapid decline in oyster reefs: effects of durable substrate on oyster populations, elevations, and aquatic bird community composition. J. Shellfish. Res. 35, 359–367.

Grabowski, J.H., 2004. Habitat complexity disrupts predator-prey interactions but not the tropic cascade on oyster reefs. Ecology 85, 995–1004. https://doi.org/10.1890/03-0067.

Grabowski, J.H., Peterson, C.H., 2007. Restoring oyster reefs to recover ecosystem services. In: Cuddington, K., Byers, J.E., Wilson, W.G., Hastings, A. (Eds.), Ecosystem Engineers, Plants to Protists, 1st ed. Elsevier Academic Press, Burlington, MA, USA, pp. 281–298.

Guerra-Chanis, G.E., Reyes-Merlo, M.Á., Díez-Minguito, M., Valle-Levinson, A., 2019. Saltwater intrusion in a subtropical estuary. Estuar. Coast. Shelf Sci. 217, 28–36.

Hair, J.F.; Black, W.C.; Babin, B.J. *Multivariate Data Analysis: A Global Perspective*; Hair, J. F., Ed.; 7. ed., global ed.; Pearson: Upper Saddle River, NJ Munich, 2010; ISBN 9780135153093.

Hall-Beyer, M., 2017. Practical guidelines for choosing GLCM textures to use in landscape classification tasks over a range of moderate spatial scales. Int. J. Remote Sens. 38, 1312–1338. https://doi.org/10.1080/01431161.2016.1278314.

Hall-Beyer, M. GLCM Texture: A Tutorial v. 3.0, University of Calgary, March 2017. 76.
Hanke, M., Posey, M., Alphin, T., 2017. The influence of habitat characteristics on intertidal oyster crassostrea virginica populations. Mar. Ecol. Prog. Ser. 571, 121–138.
Haralick, R.M., Shanmugam, K., Dinstein, I., 1973. Textural features for image classification. IEEE Trans. Syst., Man, Cybern. SMC-3, 610–621. https://doi.org/10.1109/TSMC.1973.4309314.
Harborne, A.R., Mumby, P.J., Ferrari, R., 2012. The effectiveness of different meso-scale rugosity metrics for predicting intra-habitat variation in coral-reef fish assemblages. Environ. Biol. Fish 94, 431–442.
Hengl, T.; Reuter, H.I. *Geomorphometry: Concepts, Software, Applications*; Elsevier, 2008; ISBN 978-0-08-092188-4.
Hijmans, R. (2022). terra: Spatial Data Analysis. R package version 1.6-17, <https://CRAN.R-project.org/package=terra>.
Hogan, S., Reidenbach, M.A., 2019. Quantifying and mapping intertidal oyster reefs utilizing LiDAR-based remote sensing. Mar. Ecol. Prog. Ser. 630, 83–99.
Horn, B.K.P., 1981. Hill shading and the reflectance map. Proc. IEEE 69, 14–47. https://doi.org/10.1109/PROC.1981.11918.
Howie, A.H., Bishop, M.J., 2021. Contemporary oyster reef restoration: Responding to a changing world. Front. Ecol. Evol. 9, 689915 https://doi.org/10.3389/fevo.2021.689915.
Iglhaut, J., Cabo, C., Puliti, S., Piermattei, L., O'Connor, J., Rosette, J., 2019. Structure from motion photogrammetry in forestry: A review. Curr Forestry Rep 5, 155–168. https://doi.org/10.1007/s40725-019-00094-3.
A.R. Ilich B. Misiuk V. Lecours S.A. Murawski MultiscaleDTM 2021 https://github.com/ailich/MultiscaleDTM.
Isenburg, M. (2014). LAStools—efficient LiDAR processing software. *Available online: lastools. Org.*
Jain, G.C., Consul, P.C., 1971. A generalized negative binomial distribution. SIAM J. Appl. Math. 21, 501–513.
James, M.R., Robson, S., 2012. Straightforward reconstruction of 3D surfaces and topography with a camera: accuracy and geoscience application. J. Geophys. Res. Earth 117.
Jenness, J.S., 2004. Calculating landscape surface area from digital elevation models. Wildl. Soc. Bull. 32, 829–839.
Johnson, F.A., Pine III, W.E., Camp, E.V., 2022. A cautionary tale: management implications of critical transitions in oyster fisheries. Can. J. Fish. Aquat. Sci. 79, 1269–1281. https://doi.org/10.1139/cjfas-2021-0133.
Johnston, D.W., 2019. Unoccupied aircraft systems in marine science and conservation. Annu. Rev. Mar. Sci. 11, 439–463.
Kaplan, D.A., Oblabarrieta, M., Frederick, P.C., Valle-Levinson, A., 2016. Freshwater detention by oyster reefs: quantifying a keystone ecosystem service. PLoS One 11.
Kim, K.; Lecours, V.; Frederick, P.C. Using 3D micro-geomorphometry to quantify interstitial spaces of an oyster cluster. In *Proceedings of the Geomorphometry 2018 Conference*; Guth, P; Grohmann, C.H., Peckham, S., Eds., 2018.
La Peyre, M.K., Marshall, D.A., Buie, S.C.L., Hijuelos, A., Steyer, G.D., 2022. Are we falling short on restoring oysters at a regional scale? Environ. Manag. 70, 581–592. https://doi.org/10.1007/s00267-022-01691-y.
Lavan, B. Examining the Effect of Interstitial Space on Eastern Oysters (Crassostrea Virginica): Applications of Photogrammetry and Three-Dimensional Modeling. **2019**, *Masters Theses*. 615.
Lecours, V.; Espriella, M. Can multiscale roughness help computer-assisted identification of coastal habitats in florida? In *Proceedings of the Geomorphometry 2020 Conference*; 111-114, 2020.
Lecours, V., Devillers, R., Schneider, D.C., Lucieer, V.L., Brown, C.J., Edinger, E.N., 2015. Spatial scale and geographic context in benthic habitat mapping: review and future directions. Mar. Ecol. Prog. Ser. 535, 259–284.
Lecours, V., Dolan, M.F.J., Micallef, A., Lucieer, V., 2016. A review of geomorphometry, the quantitative study of the seafloor. Hydrol. Earth Syst. Sc. 20, 3207–3244.
Lecours, V., Devillers, R., Lucieer, V.L., Brown, C.J., 2017. Artefacts in marine digital terrain models: a multiscale analysis of their impact on the derivation of terrain attributes. IEEE Trans. Geosci. Remote Sens. 55, 5391–5406.
Light, H.M.; Darst, M.R.; Lewis, L.J. Hydrology, Vegetation, and Soils of Riverine and Tidal Floodplain Forests of the Lower Suwannee River, Florida and Potential Impacts of Flow Reductions; Professional Paper; U.S. Geological Survey, 2002.
Lindsay, J.B., 2016. Whitebox GAT: a case study in geomorphometric analysis. Comput. Geosci. 95, 75–84.
Lindsay, J.B., Cockburn, J.M.H., Russell, H.A.J., 2015. An integral image approach to performing multi-scale topographic position analysis. Geomorphology 245, 51–61.
Lipcius, R.N., Burke, R.P., McCulloch, D.N., Schreiber, S.J., Schulte, D.M., Seitz, R.D., Shen, J., 2015. Overcoming restoration paradigms: value of the historical record and metapopulation dynamics in native oyster restoration. Front. Mar. Sci. 2 https://doi.org/10.3389/fmars.2015.00065.
Liu, K., Ding, H., Tang, G., Zhu, A.-X., Yang, X., Jiang, S., Cao, J., 2017. An object-based approach for two-level gully feature mapping using high-resolution DEM and imagery: a case study on hilly loess plateau region, China. Chin. Geogr. Sci. 27, 415–430. https://doi.org/10.1007/s11769-017-0874-x.
Main, M.B., Allen, G.M., 2007. Florida's environment: north central region. Wildlife Ecology and Conservation Department, Florida Cooperative Extension Service, Institute of Food and Agricultural Sciences. University of Florida, Gainesville.
Margiotta, A.M., Shervette, V.R., Hadley, N.H., Plante, C.J., Wilber, D.H., 2016. Species-specific responses of resident crabs to vertical habitat complexity on intertidal oyster reefs. J. Exp. Mar. Biol. Ecol. 477, 7–13.
McGarigal, K., Tagil, S., Cushman, S.A., 2009. Surface metrics: an alternative to patch metrics for the quantification of landscape structure. Landsc. Ecol. 24, 433–450.
Misiuk, B., Lecours, V., Bell, T., 2018. A multiscale approach to mapping seabed sediments. PLoS One 13.
Misiuk, B., Lecours, V., Dolan, M.F.J., Robert, K., 2021. Evaluating the suitability of multi-scale terrain attribute calculation approaches for seabed mapping applications. Mar. Geod. 44, 327–385.
Mitchell, B., Fisk, H., Clark, J., Rounds, E., 2018. *Lidar acquisition specifications for forestry applications*; United States department of agriculture. Geospatial Technology & Applications Center.
Moore, J.F., Pine, W.E., Frederick, P.C., Beck, S., Moreno, M., Dodrill, M.J., Boone, M., Sturmer, L., Yurek, S., 2020. Trends in oyster populations in the northeastern gulf of Mexico: an assessment of river discharge and fishing effects over time and space. Mar Coast Fish 12, 191–204. https://doi.org/10.1002/mcf2.10117.
Moore, J.L., Puckett, B.J., Schreiber, S.J., 2018. Restoration of eastern oyster populations with positive density dependence. Ecol. Appl. 28, 897–909. https://doi.org/10.1002/eap.1694.
National Academies of Sciences, Engineering, and Medicine *Effective Monitoring to Evaluate Ecological Restoration in the Gulf of Mexico*; National Academies Press: Washington, D.C., 2017; p. 23476; ISBN 978-0-309-44037-0.
Nestlerode, J.A., Luckenbach, M.W., O'Beirn, F.X., 2007. Settlement and survival of the oyster crassostrea virginica on created oyster reef habitats in chesapeake bay. Restor. Ecol. 15, 273–283.
NOAA Tides and Currents. https://tidesandcurrents.noaa.gov/stations.html?type=Water+Level+Reports (accessed on 26 February 2021).
Nugraha, W.A., Mubarak, F., Husaini, E., Evendi, H., 2020. The correlation of coral reef cover and rugosity with coral reef fish density in east java waters. JIPK 12, 131–139.
Pearson, K., Henrici, F.R.S., 1895. Contributions to the mathematical theory of evolution.—II. skew variation in homogeneous material. Philos. Trans. R. Soc. London (A.) 186, 343–414.
Pike, R.J., Wilson, S.E., 1971. Elevation-relief ratio, hypsometric integral, and geomorphic area-altitude analysis. GSA Bull. 82, 1079–1084.
Pine, W.E., Johnson, F.A., Frederick, P.C., Coggins, L.G., 2022. Adaptive management in practice and the problem of application at multiple scales—Insights from oyster reef restoration on Florida's Gulf coast. Mar. Coast. Fish. 14 https://doi.org/10.1002/mcf2.10192.
Pine, W.E., Walters, C.J., Camp, E.V., Bouchillon, R., Ahrens, R., Sturmer, L., Berrigan, M.E., 2015. The curious case of eastern oyster crassostrea virginica stock status in apalachicola bay, Florida. art46 E&S 20. https://doi.org/10.5751/ES-07827-200346.
Pittman, S.J., Christensen, J.D., Caldow, C., Menza, C., Monaco, M.E., 2007. Predictive mapping of fish species richness across shallow-water seascapes in the caribbean. Ecol. Model. 204, 9–21. https://doi.org/10.1016/j.ecolmodel.2006.12.017.
R Core Team (2021). R: A language and environment for statistical computing. R Foundation for Statistical Computing, Vienna, Austria. URL https://www.R-project.org/.
Radabaugh, K.R.; Geiger, S.P.; Moyer, P.P. *Oyster Integrated Mapping and Monitoring Program Report for the State of Florida*; FWRI Technical Report No. 22; Fish and Wildlife Research Institute, Florida Fish and Wildlife Conservation Commission: St. Petersburg, FL, USA, 2019.
Resop, J.P., Lehmann, L., Hession, W.C., 2019. Drone laser scanning for modeling riverscape topography and vegetation: comparison with traditional aerial lidar. Drones 3, 35. https://doi.org/10.3390/drones3020035.
Ridge, J.T.; DiGiacomo, A.E.; Rodriguez, A.B.; Himmelstein, J.D.; Johnston, D.W. Comparison of 3D Structural Metrics on Oyster Reefs Using Unoccupied Aircraft Photogrammetry and Terrestrial LiDAR across a Tidal Elevation Gradient. *Remote Sens Ecol Conserv* **2023**, rse2.324, doi:10.1002/rse2.324.
Ridge, J.T., Rodriguez, A.B., Joel Fodrie, F., Lindquist, N.L., Brodeur, M.C., Coleman, S.E., Grabowski, J.H., Theuerkauf, E.J., 2015. Maximizing oyster-reef growth supports green infrastructure with accelerating sea-level rise. Sci. Rep. 5, 14785.
Ridge, J.T., Gray, P.C., Windle, A.E., Johnston, D.W., 2020. Deep learning for coastal resource conservation: automating detection of shellfish reefs. Remote Sens. Ecol. Conserv. 6, 431–440.
Riley, S.J., DeGloria, S.D., Elliot, R., 1999. A terrain ruggedness index that quantifies topographic heterogeneity. Intermountain J. Sci. 5, 23–27.
Rodriguez, A.B., Fodrie, F.J., Ridge, J.T., Lindquist, N.L., Theuerkauf, E.J., Coleman, S.E., Grabowski, J.H., Brodeur, M.C., Gittman, R.K., Keller, D.A., et al., 2014. Oyster reefs can outpace sea-level rise. Nature Clim. Change 4, 493–497.
Sappington, J.M., Longshore, K.M., Thompson, D.B., 2007. Quantifying landscape ruggedness for animal habitat analysis: a case study using bighorn sheep in the mojave desert. J. Wildl. Manag. 71, 1419–1426.
Schulte, D.M., Burke, R.P., Lipcius, R.N., 2009. Unprecedented restoration of a native oyster metapopulation. Science 325, 1124–1128. https://doi.org/10.1126/science.1176516.
Seavey, J.R., Pine III, W.E., Frederick, P.C., Sturmer, L., Berrigan, M., 2011. Decadal changes in oyster reefs in the Big Bend of Florida's Gulf Coast. Ecosphere.
Soniat, T.M., Finelli, C.M., Ruiz, J.T., 2004. Vertical structure and predator refuge mediate oyster reef development and community dynamics. J. Exp. Mar. Biol. Ecol. 310, 163–182.
Sonnier, J.M., 2006. Influence of Habitat Complexity in Structuring Species-Specific Interactions and Trophic Linkages on Oyster Reefs of Southeastern North Carolina. Masters Thesis, University of North Carolina Wilmington, North Carolina, USA.
Tolley, S.G., Volety, A.K., 2005. The role of oysters in habitat use of oyster reefs by resident fish and decapod crustaceans. J. Shellfish Res. 24, 1007–1012.
Trevisani, S., Guth, P., Teza, G., 2022. A simplified geostatistical approach for characterizing key aspects of short-range roughness. SSRN J. https://doi.org/10.2139/ssrn.4223135.

Trevisani, S., Rocca, M., 2015. MAD: robust image texture analysis for applications in high resolution geomorphometry. Comput. Geosci. 81, 78–92. https://doi.org/10.1016/j.cageo.2015.04.003.

Tuckney, T.D., Dehaven, M., 2006. Fish assemblages found in tidal-creek and seagrass habitats in the suwannee river estuary. Fish. Bull. 104, 102–117.

USGS. Topographic Data Quality Levels (QLs) | U.S. Geological Survey Available online: https://www.usgs.gov/3d-elevation-program/topographic-data-quality-levels-qls (accessed on 7 February 2023).

Venables, W.N., Ripley, B.D., 2002. Random and mixed effects. In: Venables, W.N., Ripley, B.D. (Eds.), Modern Applied Statistics with S. New York, NY, Statistics and Computing; Springer, pp. 271–300.

Walbridge, S., Slocum, N., Pobuda, M., Wright, D.J., 2018. Unified geomorphological analysis workflows with benthic terrain modeler. Geosciences 8, 94.

Wallace, L.; Lucieer, A.; Watson, C. Assessing the feasibility of UAV-based lidar for high resolution forest change detection. *ISPRS - International Archives of the Photogrammetry, Remote Sensing and Spatial Information Sciences* **2012**, *XXXIX-B7*, 499–504.

Whitman, E., Reidenbach, M., 2012. Benthic flow environments affect recruitment of crassostrea virginica larvae to an intertidal oyster reef. Mar. Ecol. Prog. Ser. 463, 177–191.

Wilberg, M.J., Wiedenmann, J.R., Robinson, J.M., 2013. Sustainable exploitation and management of autogenic ecosystem engineers: application to oysters in chesapeake bay. Ecol. Appl. 23, 766–776. https://doi.org/10.1890/12-0563.1.

Windle, A.E., Poulin, S.K., Johnston, D.W., Ridge, J.T., 2019. Rapid and accurate monitoring of intertidal oyster habitat using unoccupied aircraft systems and structure from motion. Remote Sens. Environ. 11.

Windle, A.E., Puckett, B., Huebert, K.B., Knorek, Z., Johnston, D.W., Ridge, J.T., 2022. Estimation of intertidal oyster reef density using spectral and structural characteristics derived from unoccupied aircraft systems and structure from motion photogrammetry. Remote Sens. (Basel) 14, 2163.

Xiao, W., Zaforemska, A., Smigaj, M., Wang, Y., Gaulton, R., 2019. Mean shift segmentation assessment for individual forest tree delineation from airborne lidar data. Remote Sens. (Basel) 11, 1263. https://doi.org/10.3390/rs11111263.

ESRI ArcGIS Pro v 2.4 [computer software] https://pro.arcgis.com/es/pro-app.

Yanalak, M., Baykal, O., 2003. Digital elevation model based volume calculations using topographical Data. J. Surv. Eng. 129, 56–64.

Zevenbergen, L.W., Thorne, C.R., 1987. Quantitative analysis of land surface topography. Earth Surf. Proc. Land. 12, 47–56.

Zhu, H., Xu, Y., Cheng, Y., Liu, H., Zhao, Y., 2019. Landform classification based on optimal texture feature extraction from DEM data in shandong hilly area, China. Front. Earth Sci. 13, 641–655. https://doi.org/10.1007/s11707-019-0751-2.

Zvoleff A (2020). glcm: Calculate Textures from Gray-Level Co-Occurrence Matrices (GLCMs) . R package version 1.6.5, <https://CRAN.R-project.org/package=glcm>.